IEEE Access
Multidisciplinary | Rapid Review | Open Access Journal

Received 9 June 2024, accepted 21 June 2024, date of publication 24 June 2024, date of current version 2 July 2024.

Digital Object Identifier 10.1109/ACCESS.2024.3418894

THEORY

Design Technique of Open-Slot Surface-Mounted PM Machines Using Coenergy-Based Subdomain Model and Teaching-Learning-Based Optimization Algorithm

DO HYEON LEE, (Student Member, IEEE), AND SEUN GUY MIN, (Member, IEEE)
Department of Electrical Engineering, Soongsil University, Seoul 06978, South Korea
Corresponding author: Seun Guy Min (sgmin19@ssu.ac.kr)

ABSTRACT The open-slot stator topology, which allows for preformed coils and an excellent fill factor, has been regarded as a suitable candidate for low-speed operation such as direct-drive systems. This paper presents a rapid and accurate design optimization of surface-mounted permanent magnet (PM) machines equipped with the open-slot stator configuration. The analytical method, utilizing the coenergy-based subdomain model, is developed to predict the various electromagnetic performances. The proposed analytical model is decoupled into two components, relevant and irrelevant to the optimization process. Subsequently, the teaching-learning-based optimization (TLBO), a human-based algorithm for global solutions, is applied to the analytical model to search for the best compromise belonging to the Pareto-optimal front. The design methodology presented in this article is well-suited for the open-slot stator configuration, providing a computationally efficient and accurate approach to address multi-constrained minimization problems. In the end, the reliability of the proposed model is verified by finite element (FE) results.

INDEX TERMS Analytical models, coenergy principle, direct drive, open-slot stator, optimization, subdomain model, surface-mounted permanent magnet, teaching learning based optimization.

I. INTRODUCTION

Thanks to the technical advancement of power electronics, permanent magnet synchronous machines (PMSMs) have been widely used in various industries [1], [2], [3], [4]. In particular, the PMSMs equipped with fractional-slot concentrated windings (FSCW) have been gaining great interest, especially in low-speed direct-drive applications [5], due to their short end-winding, high slot fill factor, high torque density, low cogging torque, and flux weakening capability [6], [7], [8].

To date, most research works on FSCW-PMSMs have been highly focused on the semi-closed (i.e., coffin-shaped) slot configurations [9], [10], [11], [12], [13], [14], [15], [16], [17], [18], [19], [20], [21], [22], [23], [24], [25], [26], [27], [28], [29], [30], [31], which is the most common shape of stator slots. These studies can be classified by cogging torque [9], [10], [11], [12], torque pulsation [13], [14], [15], cost reduction [16], [17], radial vibration force [18], [19], [20], design analysis [21], [22], [23], [24], design optimization [25], [26], [27], [28], [29], and loss/thermal analysis [30], [31]. In contrast, limited attention has been given to research on FSCW-PMSMs with the open-slot configuration.

The open-slot structure has been regarded as a minor type of machine topology because it is connected with high levels of space harmonic and eddy-current losses, resulting in unfavorable performance at high-speed applications [32]. However, open-slot FSCW-PMSMs have their own merits in that 1) it facilitates the stator assembly using prefabricated coils, leading to an excellent fill factor and high torque density; 2) the low levels of winding inductance can be

The associate editor coordinating the review of this manuscript and approving it for publication was R. K. Saket.

achieved by eliminating tooth-tips, preventing magnetic saturation at high current ratings; 3) the torque pulsation can be minimized due to significantly reduced harmonics of the slot opening factor. Considering these characteristics, open-slot FSCW-PMSMs can be a perfect solution for direct-drive systems requiring low-speed, high-torque, and high-accuracy applications, such as robotics, electric propulsion, and wind power.

To the best of our knowledge, the research works related to the open-slot FSCW-PMSMs have been found in [32], [33], [34], and [35]. A comparative study for semi-closed and open-slot configurations was made in [32] based on several computations by the finite element (FE) method. The analytical thermal model of open-slot FSCW-PMSMs was developed in [33] by employing a lumped-parameter circuit technique. In [34], the attributes of the six different pole-slot configurations were investigated by the FE-based optimization method. The impact of the initial design decisions on the final performance of open-slot FSCW-PMSMs was discussed in [35] by using the traditional motor sizing equations. As revealed in the previous publications, there is a lack of research work on this subject. In particular, prior studies lack a computationally efficient design technique that integrates an analytical model with an optimization algorithm. Given that accurate performance prediction poses greater challenges in open-slot structures due to the leakage effects arising from the wide slot opening, a more rigorous approach should be provided for electric machine designers.

To fill this research gap, this paper presents a rapid and precise design optimization approach for surface-mounted PMSMs equipped with an open-slot FSCW configuration. Two advanced analytical methods are utilized to calculate the flux density while considering slotting effects: the subdomain (SD) model [36], [37], [38] and the complex permeance (CP) model [39], [40]. Compared with the SD model, the CP model offers quicker calculations by mapping complex geometry onto a simpler domain. However, the limitation of the CP model is based on the assumption of no shape deformation in the magnets, leading to undesired errors in flux density calculations. This drawback can be especially critical in open-slot configurations, where deformation becomes more pronounced with increasing slot opening width. For this reason, the SD model is adopted as an analytical tool in this study. Further, the developed field model is extended in two ways;

1) All electromagnetic performances can be accurately predicted using the precise method based on the magnetic coenergy. The coenergy principle enables accurate predictions in the open-slot topology without relying on approximated factor, such as slot opening factor [37], [41].
2) The analytical model is decomposed into two distinct parts, one relevant and the other irrelevant to the optimization process. As a result, the optimization procedure becomes computationally efficient, as there is no need to calculate the back-EMF and inductance.

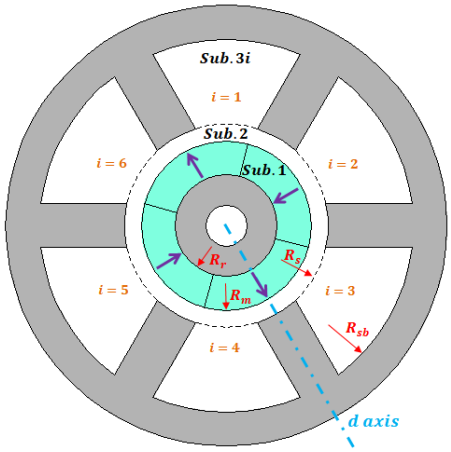

FIGURE 1. Configuration and symbols of open-slot surface-mounted PM machines.

Subsequently, a recent meta-heuristic algorithm known as Teaching Learning Based Optimization (TLBO) is employed and applied to the coenergy-based SD model to explore the best compromise within the Pareto fronts. The TLBO is a human-based algorithm inspired by the teaching and learning process in classrooms [42]. Its main advantage lies in its robustness and simplicity, as it does not require fine-tuning of algorithm parameters for optimal performance. This quality enables TLBO to overcome challenges related to parameter selection faced by well-known traditional meta-heuristics, such as genetic algorithm, particle swarm optimization, and differential evolution. Finally, a systematic optimization methodology well-suited for the open-slot stator configurations is presented, and the accuracy of the proposed model is verified by finite element (FE) results.

Demonstrating the synergy effect achieved by the combination of the coenergy-based SD model and TLBO for the optimization of open-slot PMSMs, the primary contribution of this paper lies in introducing a computationally efficient design tool ideally suited for open-slot stator configurations.

II. ANALYTICAL MODEL RELEVANT TO OPTIMIZATION

In this section, the electromagnetic performances relevant to the optimization part (i.e., electromagnetic torque, efficiency, weight, volume, and material cost) are derived using the coenergy-based SD model. The analytical field model is based on the following assumptions: 1) infinite permeability of iron materials; 2) negligible end-effects.

A. ON-LOAD FIELD MODEL

Fig. 1 illustrates the cross-section configuration and symbols of open-slot PMSMs equipped with FSCW. As shown in Fig. 1, the whole field region is classified into three types of subdomains: PMs (subdomain 1), air gap (subdomain 2), and stator slots (subdomain 3). The general solutions for the vector potential distributions in each subdomain can be

expressed by [36], [38]

$$\frac{\partial^2 A_{z1}}{\partial r^2}+\frac{1}{r}\frac{\partial A_{z1}}{\partial r}+\frac{1}{r^2}\frac{\partial^2 A_{z1}}{\partial \theta^2}=-\frac{\mu_0}{r}\left(M_\theta-\frac{\partial M_r}{\partial \theta}\right) \quad (1)$$

$$\frac{\partial^2 A_{z2}}{\partial r^2}+\frac{1}{r}\frac{\partial A_{z2}}{\partial r}+\frac{1}{r^2}\frac{\partial^2 A_{z2}}{\partial \theta^2}=0 \quad (2)$$

$$\frac{\partial^2 A_{z3}}{\partial r^2}+\frac{1}{r}\frac{\partial A_{z3}}{\partial r}+\frac{1}{r^2}\frac{\partial^2 A_{z3}}{\partial \theta^2}=-\mu_0 J \quad (3)$$

where r and θ are the radial and tangential static positions, A_{z1}, A_{z2}, and A_{z3} are z-axis components of the vector potential in the domain of magnet, air, and stator slot, respectively, μ_0 is the air permeability, M_r and M_θ are radial and tangential components of PM magnetization [43], and J is the current density in the stator slot (i.e., fill factor = 1) whose spatial distribution varies on the pole and slot number combinations.

By the variable separations, the vector potential in each subdomain can be obtained by [38]

$$A_{z1}=\sum_n\left[A_1\left(\frac{r}{R_m}\right)^n+B_1\left(\frac{r}{R_r}\right)^{-n}+\beta_{PMc}\right]\cos(n\theta)+\sum_n\left[C_1\left(\frac{r}{R_m}\right)^n+D_1\left(\frac{r}{R_r}\right)^{-n}+\beta_{PMs}\right]\sin(n\theta) \quad (4)$$

$$A_{z2}=\sum_n\left[A_2\left(\frac{r}{R_s}\right)^n+B_2\left(\frac{r}{R_m}\right)^{-n}\right]\cos(n\theta)+\sum_n\left[C_2\left(\frac{r}{R_s}\right)^n+D_2\left(\frac{r}{R_m}\right)^{-n}\right]\sin(n\theta) \quad (5)$$

$$A_{z3i}=\sum_m\left[A_{3i}\left(\frac{r}{R_{sb}}\right)^{\Lambda_m}+B_{3i}\left(\frac{r}{R_s}\right)^{-\Lambda_m}+\beta_{cu1}\right]\cdot\cos\left(\Lambda_m\left(\theta-\theta_i+\frac{b_{sa}}{2}\right)\right)+\beta_{cu2}+\beta_{cu3} \quad (6)$$

where A_1, B_1, C_1, D_1, A_2, B_2, C_2, D_2, A_{3i}, and B_{3i} are the unknown coefficients to be determined, R_{sb}, R_s, R_m, R_r are radii of stator slot bottom, stator inner, magnet, and rotor yoke surfaces, respectively, $\Lambda_m = m\pi/b_{sa}$, b_{sa} is the angle of slot width, β_{PMc} and β_{PMs} are particular solutions due to PMs, β_{cu1}, β_{cu2}, and β_{cu3} are particular solutions due to the current density, and θ_i is the center positions of the ith stator slot.

Based on (4)-(6), the general expressions of radial and tangential flux densities in each subdomain can be expressed by

$$B_{1r}=-\sum_n n\left[\frac{A_1}{r}\left(\frac{r}{R_m}\right)^n+\frac{B_1}{r}\left(\frac{r}{R_r}\right)^{-n}+\frac{\beta_{PMc}}{r}\right]\cdot\sin(n\theta)+\sum_n n\left[\frac{C_1}{r}\left(\frac{r}{R_m}\right)^n+\frac{D_1}{r}\left(\frac{r}{R_r}\right)^{-n}+\frac{\beta_{PMs}}{r}\right]\cdot\cos(n\theta) \quad (7)$$

$$B_{1\theta}=-\sum_n n\left[\frac{A_1}{r}\left(\frac{r}{R_m}\right)^n-\frac{B_1}{r}\left(\frac{r}{R_r}\right)^{-n}+\frac{\beta_{PMc}}{nr}\right]\cdot\cos(n\theta)-\sum_n n\left[\frac{C_1}{r}\left(\frac{r}{R_m}\right)^n-\frac{D_1}{r}\left(\frac{r}{R_r}\right)^{-n}+\frac{\beta_{PMs}}{nr}\right]\sin(n\theta) \quad (8)$$

$$B_{2r}=-\sum_n n\left[\frac{A_2}{r}\left(\frac{r}{R_s}\right)^n+\frac{B_2}{r}\left(\frac{r}{R_m}\right)^{-n}\right]\sin(n\theta)+\sum_n n\left[\frac{C_2}{r}\left(\frac{r}{R_s}\right)^n+\frac{D_2}{r}\left(\frac{r}{R_m}\right)^{-n}\right]\cos(n\theta) \quad (9)$$

$$B_{2\theta}=-\sum_n n\left[\frac{A_2}{r}\left(\frac{r}{R_s}\right)^n-\frac{B_2}{r}\left(\frac{r}{R_m}\right)^{-n}\right]\cos(n\theta)-\sum_n n\left[\frac{C_2}{r}\left(\frac{r}{R_s}\right)^n-\frac{D_2}{r}\left(\frac{r}{R_m}\right)^{-n}\right]\sin(n\theta) \quad (10)$$

$$B_{3r}=-\sum_m \Lambda_m\left[\frac{A_{3i}}{r}\left(\frac{r}{R_{sb}}\right)^{\Lambda_m}+\frac{B_{3i}}{r}\left(\frac{r}{R_s}\right)^{-\Lambda_m}+\frac{\beta_{cu1}}{r}\right]\cdot\sin\left(\Lambda_m\left(\theta-\theta_i+\frac{b_{sa}}{2}\right)\right) \quad (11)$$

$$B_{3\theta}=-\sum_m \Lambda_m\left[\frac{A_{3i}}{r}\left(\frac{r}{R_{sb}}\right)^{\Lambda_m}-\frac{B_{3i}}{r}\left(\frac{r}{R_s}\right)^{-\Lambda_m}+\frac{2\beta_{cu1}}{\Lambda_m r}\right]\cdot\cos\left(\Lambda_m\left(\theta-\theta_i+\frac{b_{sa}}{2}\right)\right)-\frac{\beta_{cu2}}{r\ln r}-\frac{2\beta_{cu3}}{r} \quad (12)$$

The detailed process of deriving the unknown coefficients is provided in the Appendix.

B. ELECTROMAGNETIC TORQUE

The magnetic coenergy stored in each subdomain can be calculated by the flux densities derived in (7)-(12), as given by

$$W_{PM}=\frac{L}{2\mu_0}\int_{R_r}^{R_m}\int_0^{2\pi}\left(B_{1r}^2+B_{1\theta}^2\right)d\theta dr \quad (13)$$

$$W_g=\frac{L}{2\mu_0}\int_{R_m}^{R_s}\int_0^{2\pi}\left(B_{2r}^2+B_{2\theta}^2\right)d\theta dr \quad (14)$$

$$W_s=\frac{L}{2\mu_0}\sum_{i=1}^{Q_s}\int_{R_s}^{R_{sb}}\int_{\theta_i-b_{sa}/2}^{\theta_i+b_{sa}/2}\left(B_{3r}^2+B_{3\theta}^2\right)d\theta dr \quad (15)$$

$$W_t=W_{PM}+W_g+W_s \quad (16)$$

where L is the active length, Q_s is the number of slots, W_{PM}, W_g, and W_s are the magnetic coenergy stored in the magnet, air gap, and stator slot respectively, and W_t is the total magnetic coenergy stored in PM machines.

Under the condition that all three-phase currents (i.e., i_a, i_b, and i_c) are excited, the electromagnetic torque, including the cogging torque, can be obtained by the derivative of the total magnetic coenergy with respect to the rotor angular position:

$$T_{em}(\Theta)=\partial W_t(\Theta)/\partial\Theta \quad (17)$$

where T_{em} is the electromagnetic torque and Θ is the rotational angle between the rotor magnet and the referent position.

By utilizing the Fourier transform, (17) can be written in the form of Fourier series, as follows:

$$T_{em}(\Theta) = T_{avg} + \sum_{h} T_{r(6h)} \cos(6hp\Theta) \tag{18}$$

where T_{avg} is the average torque (i.e., fundamental component of T_{em}), T_r is the torque ripple component (i.e., harmonic components of T_{em}), and p is the number of pole pairs.

It should be noted that T_r includes both the cogging component and harmonic mismatch component between the back-EMF shape and the current.

C. TOOTH WIDTH AND BACK IRON THICKNESS

The tooth width and back iron thickness are crucial parameters in the optimization process, especially in the open-slot structure, because their values must be selected to keep the flux density below the saturation level of the ferromagnetic material. The maximum flux density in the tooth and back iron can be calculated by

$$B_t = \phi_{sm}/T_w L \tag{19}$$

$$B_{sb} = \phi_{sm}/y_{sb} L \tag{20}$$

$$B_{rb} = \phi_{rm}/y_{rb} L \tag{21}$$

where B_t, B_{sb}, and B_{rb} are the maximum flux densities in the tooth, stator back iron, and rotor back iron, respectively, T_w is the tooth width, y_{sb} is the stator back iron thickness, y_{rb} is the rotor back iron thickness, ϕ_{sm} is the maximum flux traveling through the stator tooth, and ϕ_{rm} is the maximum flux traveling through the rotor yoke.

Under the condition that all three-phase currents are energized, ϕ_{sm} and ϕ_{rm} can be calculated by the integration of the surface surrounded by the slot and magnet, respectively:

$$\phi_{sm} = \max\left[L \int_{R_s}^{R_{sb}} \left(B_{3r}(\Theta)|_{\theta=\theta_\alpha} + B_{3r}(\Theta)|_{\theta=\theta_\beta} \right) dr + LR_s \int_{\theta_\alpha}^{\theta_\beta} B_{2r}(\Theta)|_{r=R_s}\, d\theta \right] \tag{22}$$

$$\phi_{rm} = \max\left[LR_r \int_{\theta_{PM}-\pi/2p}^{\theta_{PM}+\pi/2p} B_{1r}(\Theta)|_{r=R_r}\, d\theta \right] \tag{23}$$

where $\boldsymbol{\theta_\alpha} = \boldsymbol{\theta_i} + \boldsymbol{b_{sa}/2}$, $\boldsymbol{\theta_\beta} = \boldsymbol{\theta_{i+1}} - \boldsymbol{b_{sa}/2}$, and $\boldsymbol{\theta_{PM}}$ is the center position of the rotor magnet. This approach provides more accurate calculation of $\boldsymbol{\phi_{sm}}$ in open-slot configuration by considering the flux densities through the side aspect of the tooth.

D. LOSS AND EFFICIENCY

As stated in the Introduction, the open-slot stator configuration is adopted in low-speed applications due to its intrinsic characteristics. Consequently, the copper loss becomes the predominant component in this machine topology. The formulation for the copper loss can be expressed as follows:

$$P_{cu} = 3 I_{ph}^2 R_{cu} \tag{24}$$

where I_{ph} is the root mean square (RMS) value of the phase current and R_{cu} is the phase resistance of the copper winding.

The phase resistance of copper winding can be expressed as

$$R_{cu} = \rho_{cu} \frac{n_c N_c 2(L + l_{end})}{A_s f_f / N_c} \tag{25}$$

where ρ_{cu} is the copper resistivity, n_c is the number of coils per phase, N_c is the number of winding turns per coil, l_{end} is the mean length of the end-turn on one side of the coil, A_s is the slot area per layer, and f_f is the fill factor.

The phase current can be given by

$$I_{ph} = \frac{A_s f_f J_{cu}}{N_c} \tag{26}$$

where J_{cu} is the current density of the stator conductor in RMS value (i.e., $J_{cu} = J/f_f$).

Substituting (25) and (26) into (24) yields

$$\begin{aligned} P_{cu} &= 3 \left(\frac{A_s f_f J_{cu}}{N_c} \right)^2 \rho_{cu} \frac{n_c N_c 2(L + l_{end})}{A_s f_f / N_c} \\ &= 6 A_s f_f J_{cu}^2 \rho_{cu} n_c (L + l_{end}) \end{aligned} \tag{27}$$

At higher speeds, the other power loss components become more significant. These include the core loss in the stator lamination, eddy-current losses induced by PMs and conductors, and mechanical loss. However, given that the open-slot stator topology is intended for low-speed applications, the eddy-current losses and mechanical loss can be neglected in the loss calculation. Therefore, the efficiency can be calculated by

$$\eta = \frac{T_{avg} w_r}{T_{avg} w_r + P_{cu} + P_{core}} \tag{28}$$

where w_r is the mechanical rotor angular speed and P_{core} is the core loss in the stator lamination, for which the calculation technique is described in [44].

E. WEIGHT, VOLUME, AND COST

The active weight can be classified into four parts: PMs, stator iron, rotor iron, and stator conductor. The active weight can be obtained by multiplying the density with the volume:

$$\omega_{PM} = \pi \left(R_m^2 - R_r^2 \right) \alpha_p L \delta_{PM} \tag{29a}$$

$$\omega_{ri} = \pi \left(R_r^2 - (R_r - y_{rb})^2 \right) L \delta_{fe} \tag{29b}$$

$$\omega_{si} = \left[\pi \left(R_{os}^2 - R_{sb}^2 \right) + T_w h_s Q_s \right] L \delta_{fe} \tag{29c}$$

$$\omega_{cu} = 2 n_c A_s f_f (L + l_{end}) \delta_{cu} \tag{29d}$$

where α_p is the pole arc to pole pitch ratio, δ_{PM}, δ_{fe}, and δ_{cu} is the density of magnet, iron, and stator conductor, respectively, h_s is the slot height (i.e., $h_s = R_{sb} - R_s$), and R_{os} is the outer radius (i.e., $R_{os} = R_{sb} + y_{sb}$).

The volume of machine can be readily calculated by

$$V_o = \pi R_{os}^2 L \tag{30}$$

Finally, the material cost is estimated using the following basis: PMs (U.S. $125/kg), copper winding (U.S. $10/kg), and iron (U.S. $2.5/kg). Therefore, the material cost can be calculated by

$$\mathcal{E}_{cost} = 125\omega_{PM} + 10\omega_{cu} + 2.5\,(W_{ri} + W_{si}) \tag{31}$$

III. ANALYTICAL MODEL IRRELEVANT TO OPTIMIZATION

In this section, the electromagnetic parameters irrelevant to the optimization part (i.e., back-EMF, winding inductance, and number of turns) are derived by the coenergy-based SD model.

A. BACK-EMF

The conventional approach for calculating the back-EMF is based on the slot opening factor [37], [41], which enables a partial assessment of the leakage flux components traversing through the air gap. However, this method lacks the required accuracy for open-slot configurations, especially as the slot opening width increases, leading to significant errors. Therefore, in this study, a more rigorous technique is proposed for back-EMF calculation by employing magnetic coenergy principles.

Assuming that the phase B and C currents are deactivated (i.e., $i_b = i_c = 0$), the magnetic flux linkage passing through the phase A winding can be obtained as

$$\lambda_{PM-A}(\Theta) = \frac{W_t|_{PM\neq 0, i_a=I_a} - W_t|_{PM\neq 0, i_a=0} - W_t|_{PM=0, i_a=I_a}}{I_a} \tag{32}$$

where PM $= 0$ means no magnetization (i.e., turning off PMs), $PM \neq 0$ means that PMs operate normally, and I_a is the arbitrary value of phase A current.

Similarly, the magnetic flux linkage passing through the phase B and C winding can be expressed as follows:

$$\lambda_{PM-B}(\Theta) = \frac{W_t|_{PM\neq 0, i_b=I_b} - W_t|_{PM\neq 0, i_b=0} - W_t|_{PM=0, i_b=I_b}}{I_b} \tag{33}$$

$$\lambda_{PM-C}(\Theta) = \frac{W_t|_{PM\neq 0, i_c=I_c} - W_t|_{PM\neq 0, i_c=0} - W_t|_{PM=0, i_c=I_c}}{I_c} \tag{34}$$

For (33), phase A and C currents are turned off (i.e., $i_a = i_c = 0$), and for (34), phase A and B currents are turned off (i.e., $i_a = i_b = 0$).

Finally, the back-EMF for each phase can be obtained by taking the negative derivative of the magnetic flux linkage with respect to the time:

$$e_j(\Theta) = \frac{\partial \lambda_{PM-j}(\Theta)}{\partial t} = \frac{\partial \lambda_{PM-j}(\Theta)}{\partial \Theta} w_r, \; j = A, B, C \tag{35}$$

Although (35) accurately predicts the back-EMF waveform, one drawback of this method is the longer computational time it requires. This is because it requires consideration of three different conditions (i.e., $\boldsymbol{PM} = \mathbf{0}$, $\boldsymbol{I} = \mathbf{0}$, and $\boldsymbol{PM} = \boldsymbol{I} = \mathbf{0}$) to calculate one point of magnetic flux linkage. However, this limitation is not a problem in this work, as the back-EMF calculation is decoupled from the iterative optimization, which is a notable advantage of the proposed design method.

B. WINDING INDUCTANCE

The winding inductance can be straightforwardly calculated by using the magnetic coenergy. Assuming that PMs are deactivated (i.e., $PM = 0$), the magnetic coenergy for the three-phase winding can be expressed as follows:

$$W_t|_{PM=0} = \frac{1}{2}L_{aa}i_a^2 + \frac{1}{2}L_{bb}i_b^2 + \frac{1}{2}L_{cc}i_c^2 + M_{ab}i_a i_b + M_{ac}i_a i_c + M_{bc}i_b i_c \tag{36}$$

where L_{ii} is the self-inductance (i.e., $L_{ii} = L_{aa} = L_{bb} = L_{cc}$) and M_{ij} is the mutual-inductance (i.e., $M_{ij} = M_{ab} = M_{ac} = M_{bc}$).

Based on (36), the self-inductance can be calculated by injecting the current in one-phase, e.g., $i_a = I_a$ and $i_b = i_c = 0$:

$$L_{ii} = \frac{2\,W_t|_{PM=0, i_b=0, i_c=0}}{I_a^2} \tag{37}$$

Subsequently, the mutual-inductance can be obtained by injecting the current in two-phases, e.g., $i_a = I_a$, $i_b = I_b$, and $i_c = 0$:

$$M_{ij} = \frac{W_t|_{PM=0, i_c=0} - L_{ii}I_a^2/2 - L_{ii}i_b^2/2}{I_a I_b} \tag{38}$$

C. ROTATIONAL SPEED AND NUMBER OF TURNS

At the final design stage, the winding number of turns N_c is determined based on the rotational speed w_r. The voltage equation in the phase A winding can be expressed as follows:

$$v_A(\Theta) = \underbrace{e_A(\Theta)}_{\propto N_c} + \underbrace{R_{cu}i_A(\Theta)}_{\propto N_c} + \underbrace{(L_{ii} - M_{ij})\frac{di_A(\Theta)}{dt}}_{\propto N_c} \tag{39}$$

As shown in (39), all voltage terms are directly proportional to the number of turns N_c, resulting in the phase voltage v_A increasing proportionally with the number of turns N_c. Therefore, the machine designer may increase the number of turns until the phase voltage is just below the maximum voltage supplied by the inverter. This can be achieved through a straightforward iterative method. Subsequently, the corresponding conductor diameter w_d can be calculated by

$$w_d = \sqrt{\frac{4A_s f_f}{\pi N_c}} \tag{40}$$

IV. OPTIMIZATION

In this section, the Teaching Learning Based Optimization (TLBO) algorithm is implemented in the analytical model of open-slot PMSMs, as proposed in section II, to explore the optimal trade-offs within the Pareto fronts. The comprehensive and systematic optimization process is illustrated in Fig. 2.

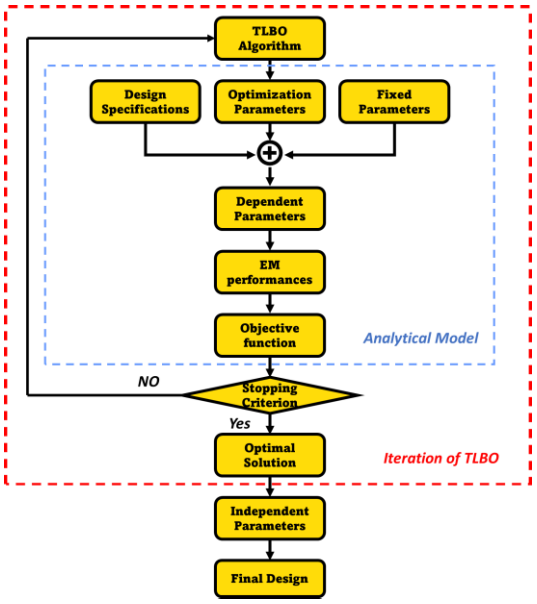

FIGURE 2. Flowchart to describe the comprehensive optimization process.

TABLE 1. Definition of five optimization parameters.

Symbol	Parameter	Unit	Initial range
D	Rotor diameter	mm	[30, 200]
h_m	Magnet thickness	mm	[1, 10]
α_p	Pole arc to pole pitch ratio	–	[0.5, 1]
h_s	Slot height	mm	[5, 30]
β_{op}	Slot opening to slot pitch ratio	–	[0.2, 0.8]

TABLE 2. Set of design requirements.

Symbol	Parameter	Unit	Value
T_{avg}	Rated torque	Nm	27
w_r	Rated speed	RPS	5
V_m	Rated voltage	V	170

A. OPTIMIZATION PROCESS

As depicted in Fig. 2, the proper selection of design specifications, optimization parameters, and fixed parameters is a prerequisite that needs to be fulfilled before commencing with the optimization process.

Table 1 shows an overview of the five structural dimensions of PMSMs selected as optimization parameters, accompanied by their initial range. Table 2 displays the design requirements for open-slot PMSMs. As mentioned in section III, the rated speed and supply voltage can be adjusted by altering the number of winding turns, which remains unaffected by the shape optimization. Consequently, during the optimization process, only the rated torque is considered. Table 3 provides an overview of the seven fixed parameters that can be predetermined by the designer. The selection of 20 poles and 18 slots is based on their advantageous properties, including a large least common multiple and low harmonic components of the magneto motive force. These characteristics help

TABLE 3. Definition of seven fixed parameters.

Symbol	Parameter	Unit	Value
N_p	Number of poles	–	20
Q_s	Number of slots	–	18
g	Air gap	mm	1
f_f	Fill factor	–	0.5
J_{cu}	Rated current density	A_{rms}/mm^2	5
B_r	Residual flux density	T	1.345
B_{sat}	Saturation flux density	T	1.7

mitigate undesirable effects such as cogging torque and torque ripple [5]. Additionally, in order to achieve superior electromagnetic performances, such as increased specific power and torque production, this article has chosen a small air gap, large fill factor, and high residual flux as the minimum and maximum allowable values within the constraints of available manufacturing technologies and material costs.

Moreover, there are several dependent parameters that are automatically determined during the optimization process. These parameters include the tooth width, yoke thickness, and active length. The calculation of the tooth width in the open-slot stator configuration can be obtained using the following geometrical relationship:

$$T_w = \tau_{slot} - b_{s0} \tag{41}$$

where τ_{slot} is the slot pitch and b_{s0} is the slot opening.

Accordingly, considering that the magnetic flux passing through the tooth width separates into two halves, with each half forming a flux loop with one-half of the flux of the adjacent magnet, the stator and rotor back iron thickness can be calculated as follows:

$$y_{sb} = y_{rb} \coloneqq T_w/2 \tag{42}$$

Meanwhile, the active length can be derived as

$$L = \frac{T_{arb}}{T_{avg}} \times L_{arb} \tag{43}$$

where L_{arb} is the active length set to an arbitrary value (i.e., initial random value) and T_{arb} is the arbitrary torque value corresponding to L_{arb}.

B. OBJECTIVE FUNCTION

Given that PMSMs are typically recommended to possess low weight, low loss, low volume, and low cost, the objective function for the minimization problem is formulated as follows:

$$f_{obj} = C_w x_w + C_l x_l + C_v x_v + C_c x_c + PF \tag{44}$$

where x_w, x_l, x_v, and x_c are active weight, total loss, volume, and cost, respectively, C_w, C_l, C_v, and C_c are weighting factors assigned to each performance index, allowing for a high degree of freedom to achieve the optimal trade-off among design objectives, and PF is a penalty function implemented to avoid solutions that violate constraints by penalizing the objective function accordingly. During the

optimization process, common constraints are applied to prevent the magnetic saturation within the core and avoid the machine size from escalating. This can be achieved by the following approach:

$$PF = \left(\frac{R_{os}}{100}\right)^{n} + \left(\frac{B_t}{B_{sat}}\right)^{n} + \left(\frac{B_{sb}}{B_{sat}}\right)^{n} + \left(\frac{B_{rb}}{B_{sat}}\right)^{n} \quad (45)$$

where $\boldsymbol{n}$ is an arbitrary large value (e.g., $\boldsymbol{n} = \boldsymbol{e^{50}}$) and $\boldsymbol{B_{sat}}$ is a saturation flux density in the iron.

C. TEACHING LEARNING BASED OPTIMIZATION

The TLBO is an efficient optimization method introduced by Rao et al. in 2011. This algorithm utilizes knowledge transfer behaviors observed between teachers and learners, making it widely applicable to solve complex optimization problems. TLBO offers simplicity and robustness, surpassing other optimization algorithms (e.g., differential evolution, particle swarm optimization, genetic algorithm) by employing only common parameters such as population size, number of variables, and iterations. Specifically, at any iteration i, there are m subjects (design variables $j = 1, 2, \cdots, m$) and n learners (population size $k = 1, 2, \cdots, n$). For this paper, the common parameters are selected as follows:

1) Population size: 5
2) The number of variable: 20
3) The number of iteration: 100

The TLBO algorithm operates in two phases: the teacher phase and the learner phase. During the teacher phase, the knowledge levels of learners (X_i) are improved using the information from the teacher (X_{best}), as shown below:

$$\Delta X = r_i(X_{best} - T_F X_{mean}) \quad (46)$$

where X_{best} is the value of the teacher, X_{mean} is the mean value of learners, r_i is the random number in the range [0, 1], T_F is the teaching factor which randomly decides the value either 1 or 2 to determine the mean value, i.e.,

$$T_F = round[1 + rand\ (0, 1)] \quad (47)$$

As a result, a new equation for solution generation is derived as follows:

$$X_i^{new} = X_i^{old} + \Delta X \quad (48)$$

The update of X_i to X_i^{new} occurs only when the objective function value of X_i^{new} shows improvement. During the learner phase, learners X_i enhance and refine their knowledge through random interactions with other learners X_j in the class, based on the outcomes of the teacher phase. The learning process for minimization problems in this phase is explained below:

$$X_i^{new} = X_i^{old} + r_i\left(X_i - X_j\right) \quad (49)$$

$$X_i^{new} = X_i^{old} - r_i\left(X_i - X_j\right) \quad (50)$$

If the objective function value of $\boldsymbol{X_i}$ is higher than $\boldsymbol{X_j}$, the knowledge level is adjusted according to (49); otherwise, it will be adjusted as per (50). In conclusion, by comparing with the original individual at every iteration, $\boldsymbol{X_i^{new}}$ is updated as the optimal value.

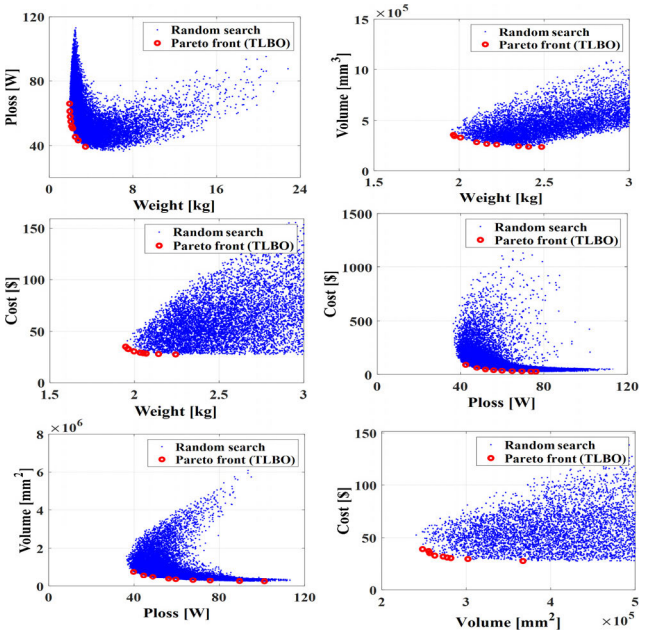

FIGURE 3. Pareto fronts resulting from the two-objective optimization problems.

D. OPTIMIZATION RESULT AND DISCUSSION

The TLBO algorithm is applied to the developed analytical model to search for the optimal solution while adhering to the common constraints specified in (45). As a result, adjusting the weighting factors yields the desired 2-D Pareto fronts, as illustrated in Fig. 3. For example, modifying C_w and C_l, with C_v and C_c set to zero, produces the Pareto front concerning weight and loss. Similarly, other Pareto fronts can be generated through suitable adjustments to the weighting factors. Simultaneously, the results of 15,000 random searches are also illustrated in Fig. 3, providing a baseline for comparison with TLBO results. As shown in Fig. 3, all random design candidates are located above the Pareto front, demonstrating the validity of the solutions found by TLBO. It is important to highlight that the optimal design values within the Pareto front, as depicted in Fig. 3, exhibit a remarkably high level of accuracy, which is attributable to the coenergy-based method proposed in this paper.

To demonstrate why the TLBO algorithm has been chosen for this study, the performance of TLBO is evaluated through a comparative analysis with four well-known meta-heuristic algorithms: differential evolution (DE), particle swarm optimization (PSO), crew search algorithm (CSA), and sine cosine algorithm (SCA). In Fig. 4, the variation of the objective function value is depicted across three different population sizes ($N = 10, 20, 30$), with a fixed number of iterations set at 100 (i.e., $i_{max} = 100$), while maintaining the all weighting factors at the same value (i.e., $C_w = C_l = C_v = C_c = 1$). As illustrated, TLBO not only achieves the lowest objective function values but also proves its effectiveness in reaching optimal solutions with faster convergence, regardless of the population size. As a consequence, TLBO

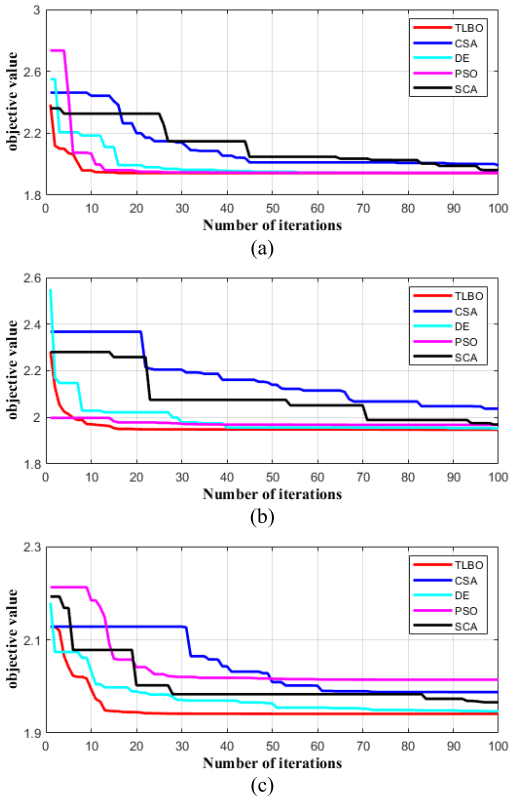

FIGURE 4. Comparison of five distinct meta-heuristic algorithms at i_{max} = 100. (a) $N = 10$. (b) $N = 20$. (c) $N = 30$.

TABLE 4. Comparison of time required for 2000 design candidates.

	Traditional Analytical	Proposed Analytical	2-D FEA
Time (s)	61560	22800	246000

outperforms other algorithms, demonstrating its primary advantages in open-slot configurations where the slot opening to slot pitch ratio plays a crucial role as an optimization parameter.

Finally, Table 4 displays a comparison of the approximate time needed to evaluate 2000 design candidates using traditional, proposed, and FE models. The traditional method involves calculating coil design components such as winding number of turns and conductor diameter during iteration, whereas the proposed method, by decoupling from optimization, eliminates the need for such calculations. This strategic exclusion significantly enhances the efficiency of the modeling process, resulting in substantial time savings, as exhibited in Table 4.

E. CORRELATION ANALYSIS

A correlation analysis of the five optimization parameters with respect to the objective function is conducted in this section. For this analysis, more than 5000 optimization data candidates have been extracted under various conditions.

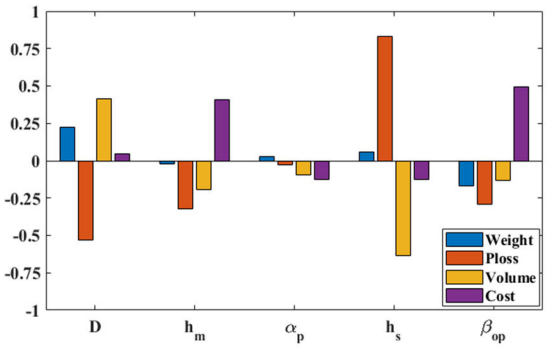

FIGURE 5. Sensitivity of the five optimization parameters with respect to the objective function.

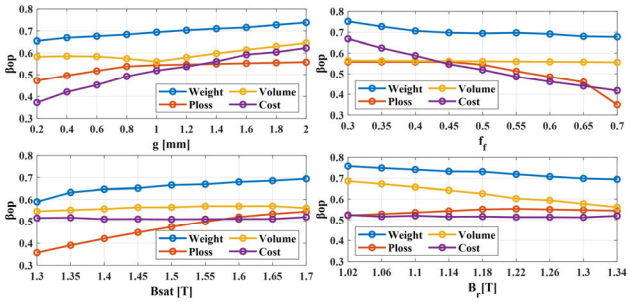

FIGURE 6. The optimal value of slot opening to slot pitch ratio in each different fixed parameters.

Specifically, optimizations are individually executed for each performance index (weight, loss, volume, and cost) while varying the fixed parameters specified in Table 3. Subsequently, sensitivity analysis is performed using the Pearson Correlation Coefficient (PCC), which ranges from −1 to 1, based on the collected optimization data. A positive PCC value signifies a positive correlation, while a negative value indicates a negative correlation. The closer the absolute value of PCC is to 1, the stronger the correlation.

Fig. 5 depicts the results of this sensitivity analysis, showing the varying degrees of sensitivity between these five optimization parameters and each performance index. As illustrated, the rotor diameter D notably impacts weight and volume positively, but it reduces loss. The magnet thickness h_m greatly increases cost, while exerting a negative impact on loss and volume. The pole arc to pole pitch ratio α_p has a modest effect on all objectives. The slot height h_s significantly influences loss positively but notably decreases volume. Finally, the slot opening to slot pitch ratio β_{op} strongly raises cost while slightly reducing weight, loss, and volume. These findings will serve as valuable reference points for optimizing open-slot FSCW-PMSMs.

Given the significance of the slot opening to slot pitch ratio β_{op} in open-slot stator configurations, a deeper exploration of this factor is conducted. As a result, Fig. 6 shows the optimal slot opening to slot pitch ratio for each performance

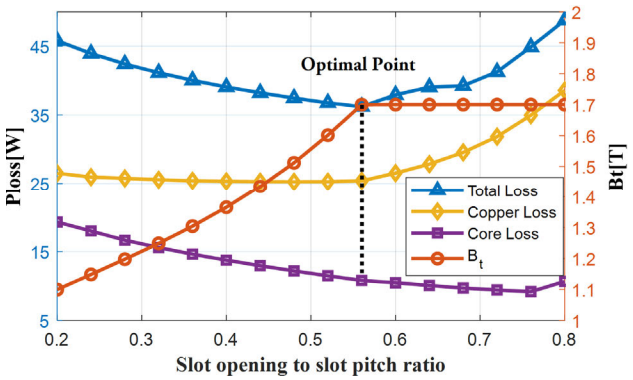

FIGURE 7. The variation of loss and flux density in the stator tooth with respect to the slot opening to slot pitch ratio.

objective, considering the variation in fixed parameters, such as air gap, fill factor, saturation flux density, and residual flux density. It is important to note that while fixed parameters maintain constant values for a particular independent design, they are not necessarily immutable in all circumstances. For example, the fill factor can vary depending on the winding method and configuration, the air gap is affected by motor manufacturing technology, and saturation flux density and residual flux density can differ based on chosen materials. Therefore, it is reasonable to analyze the effect of the slot opening to slot pitch ratio by treating fixed parameters as independent variables and varying them within specified ranges during this investigation. The insights from Fig. 6 can be summarized as follows:

- ✓ The figure clearly illustrates that the air gap has a substantial influence on the optimal value of the slot opening to slot pitch ratio for all performance objectives. Specifically, as the air gap increases, the optimal slot opening to slot pitch ratio increases in relation to all performance objectives.
- ✓ The optimal slot opening to slot pitch ratio remains constant regardless of the variation of the fill factor from the perspective of volume optimization. However, it decreases in relation to the other performance objectives.
- ✓ The optimal slot opening to slot pitch ratio remains constant regardless of the variation of the saturation flux density from the perspective of cost and volume optimization. However, it increases concerning the weight and loss optimization.
- ✓ The optimal slot opening to slot pitch ratio remains constant regardless of the variation of the residual flux density from the perspective of loss and cost optimization. However, it decreases concerning the weight and volume optimization.

Fig. 7 displays the variation of loss and tooth flux density with respect to the slot opening to slot pitch ratio. Based on Fig. 7, it becomes evident that the total loss is minimized when the tooth flux density reaches the saturation flux density (In this work, saturation flux density is set to 1.7T, as outlined in Table 3). Subsequently, the total loss increases due to the dominance of the copper loss. From these results, it can be concluded that to achieve loss minimization in an open-slot PMSM, it is crucial to select the slot opening to slot pitch ratio value at the point where the tooth flux density reaches the saturation flux density. Overall, the research findings reported in Figs 5, 6, and 7 holds significant implications for the optimization of PMSMs equipped with an open-slot stator topology.

TABLE 5. Major design parameters of validation models.

Symbol	Parameter	Model A	Model B	Model C
D	Rotor diameter	100	120	98
D_{os}	Outer diameter	138.5	164.6	136
L	Active length	35	30	60
h_m	Magnet thickness	2.5	4.5	4
α_p	Pole arc ratio	0.95	0.83	0.78
h_s	Slot height	15.5	17.5	14.5
T_w	Tooth width	3.53	8.91	6.8
$\boldsymbol{\beta_{op}}$	**Slot opening to slot pitch ratio**	**0.8**	**0.65**	**0.61**
N_p	Number of poles	12	20	20
Q_s	Number of slots	18	15	18
g	Air gap	0.5	0.8	1
f_f	Fill factor	0.5	0.55	0.5
J_{cu}	Current density	4.5	5	5
B_r	Res. flux density	0.45	1.35	1.345
N_c	Number of turns	168	152	107
w_d	Conductor diameter	0.7	0.9	0.75

V. FE VALIDATIONS

In this section, the coenergy-based analytical method proposed in this paper is validated through FE simulations. Three validation models are employed for this purpose, and the main design parameters for each of them are provided in Table 5. Subsequently, the topological structure diagrams of three validation models are illustrated in Fig. 8. All validation models have an exceptionally wide slot opening width, indicating an open-slot configuration.

As shown in Table 5, Model C aligns with the provisions outlined in Table 3. However, Model C adopts 20-poles/18-slots configuration, which inherently yields minimal harmonic components due to its distributed winding layout. Consequently, this configuration would lead to negligible levels of torque pulsation and back-EMF harmonics [45], [46], making it unsuitable for validation purposes. Therefore, Models A and B, diverging from the provisions of Table 3, have been included as validation models. These models, belonging to the 2-poles/3-slots family and 4-poles/3-slots family, respectively, are considered suitable for validation due to their tendency to exhibit more harmonic components.

Figs. 9-11 exhibit the comparison of the phase back-EMF at a speed of 500 rpm for three validation models. The slot opening factor-based conventional analytical method [37], [41] has been implemented alongside, providing a basis for the comparison. It is evident that the proposed analytical

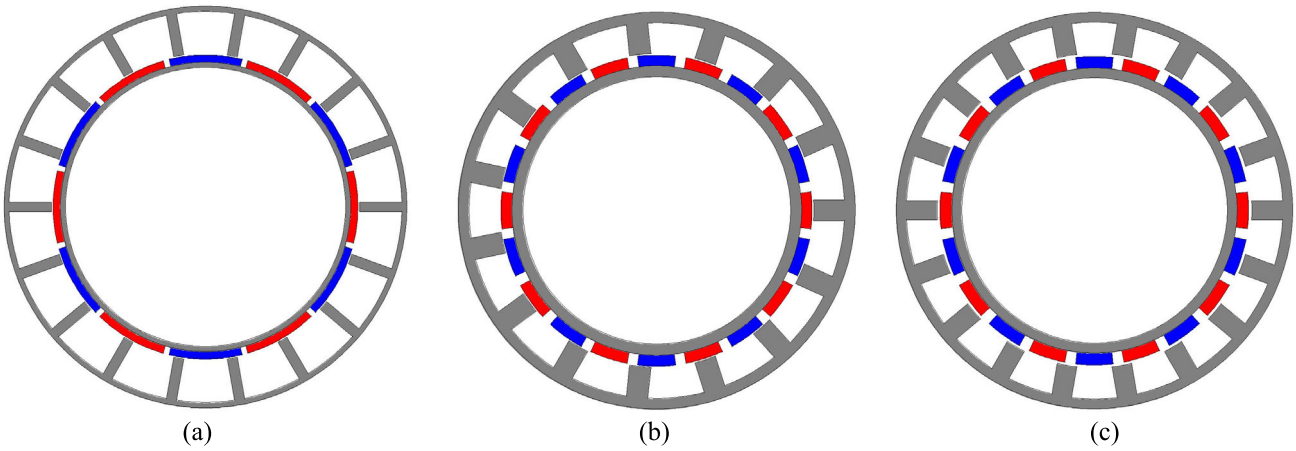

FIGURE 8. The topological structure diagram of three validation models listed in Table 5. (a) Model A. (b) Model B. (c) Model C.

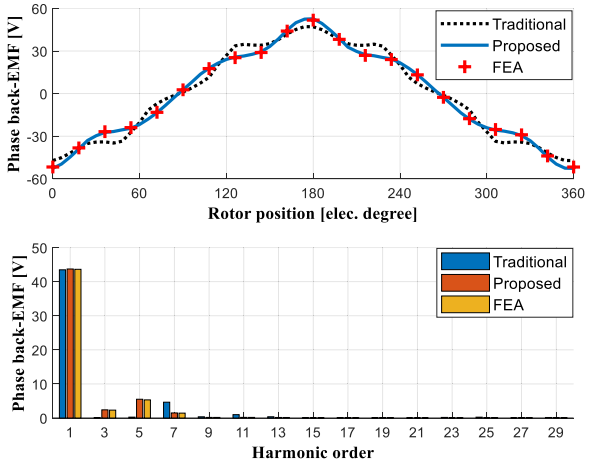

FIGURE 9. Comparison of phase back-EMF for Model A at 500 rpm.

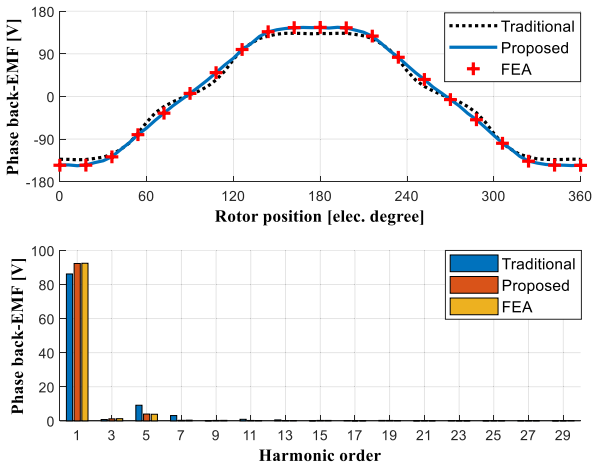

FIGURE 10. Comparison of phase back-EMF for Model B at 500 rpm.

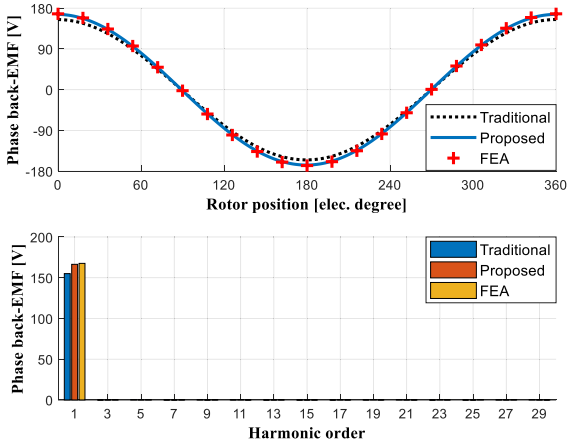

FIGURE 11. Comparison of phase back-EMF for Model C at 500 rpm.

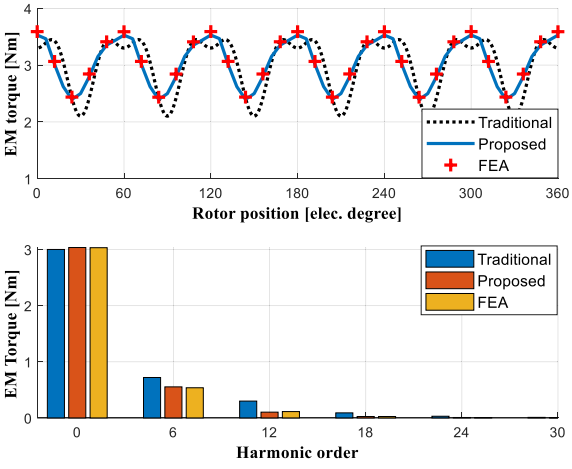

FIGURE 12. Comparison of electromagnetic torque for Model A.

results exhibit a high level of agreement with the FE results, whereas the traditional method shows some discrepancies with the FE results. These discrepancies can be attributed to the approximated evaluation of leakage effects arising from wide slot openings in the traditional method.

TABLE 6. Numerical comparison of inductance components (Unit: mH).

Inductance		Model A		Model B		Model C	
		Analytical	FEA	Analytical	FEA	Analytical	FEA
Self	Air gap	11.58	11.41	7.98	8.01	14.74	14.79
	Slot	8.10	8.02	4.19	4.13	8.69	8.62
	Total	19.68	19.43	12.17	12.14	23.43	23.41
Mutual	Air gap	-5.32	-5.37	-3.65	-3.59	-0.57	-0.55
	Slot	-3.40	-3.33	-1.72	-1.77	-0.62	-0.62
	Total	-8.72	-8.70	-5.37	-5.36	-1.19	-1.17
Phase (Self-Mutual)	Air gap	16.90	16.78	11.63	11.60	15.31	15.34
	Slot	11.50	11.35	5.91	5.90	9.31	9.24
	Total	28.40	28.13	17.54	17.50	24.62	24.58

TABLE 7. Numerical comparison of efficiency and power factor at 2000 RPM.

	Model A		Model B		Model C	
	Analytical	FEA	Analytical	FEA	Analytical	FEA
Torque [Nm]	2.99	2.98	11.18	11.09	14.94	14.97
Mechanical power [W]	626.03	624.87	1.76	1.74	2.57	2.45
Joule loss [W]	56.49	56.63	58.11	57.77	89.77	90.36
Core loss [W]	6.25	5.75	24.45	22.11	19.18	18.84
Reactive power [VAR]	321.07	318.02	0.23	0.22	0.39	0.35
Efficiency [%]	90.89	90.92	95.51	95.62	95.92	95.72
Power factor	0.906	0.908	0.888	0.890	0.870	0.880

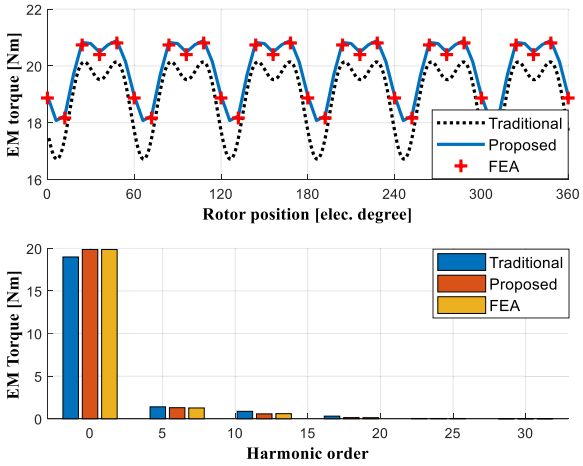

FIGURE 13. Comparison of electromagnetic torque for Model B.

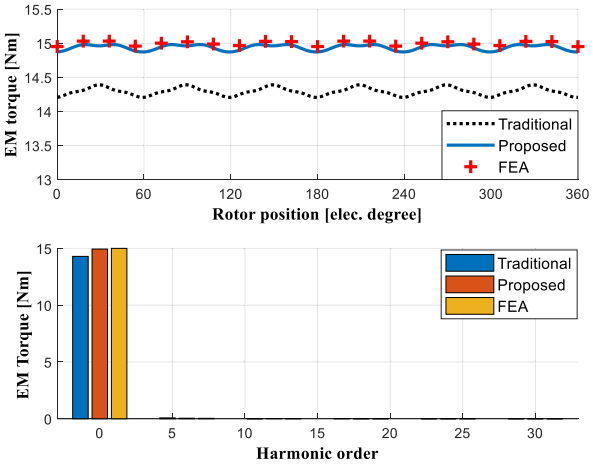

FIGURE 14. Comparison of electromagnetic torque for Model C.

Figs. 12-14 illustrate a comparison of the electromagnetic torque. Similar to the phase back-EMF, the proposed analytical method shows excellent agreement with FEA, while the conventional method exhibits some discrepancies when compared to FE results. Notably, the proposed method demonstrates a close match not only with fundamental components but also with harmonic components in FEA, as illustrated in Figs. 9-14 through the harmonic spectrum. Therefore, the coenergy-based analytical method proposed in this study is proven to be a highly reliable approach, even in situations where accurate performance prediction is more challenging, such as in open-slot configurations. Besides, when comparing Models A and B, it is evident that Model C shows minimal torque ripple and back-EMF harmonic components, as shown in Figs. 11 and 14. This can be attributed to the previously discussed 20-poles/18-slots configuration.

As shown in Figs. 9-14, the slot opening-based traditional method also yields results with a certain level of reliability, showing comparable outcomes to FEA. However, since the slot opening factor is based on the correction coefficient, it cannot accurately evaluate the leakage flux arising from the slot openings, as clearly demonstrated in Figs. 9-14. Consequently, for applications demanding precise performance prediction, such as high-precision servo motors, the proposed method holds significant research value. Furthermore, beyond its industrial relevance, proposing accurate calculation methods always carries substantial academic importance, establishing a promising design approach in the field of electric machinery.

Finally, the numerical comparisons of winding inductance are exhibited in Table 6, revealing an outstanding agreement between the proposed method and the FE results.

VI. CONCLUSION

This paper presents a rapid and accurate design optimization method for FSCW-PMSMs with an open-slot configuration, utilizing the coenergy-based subdomain model. In Sections II and III, the analytical model is systematically developed by decoupling into relevant and irrelevant components with respect to the optimization. Section IV presents a comprehensive optimization process, where the TLBO algorithm is integrated with the analytical model to explore the optimal trade-offs within the Pareto fronts. In section V, the reliability of the analytical model is verified through FE results. To summarize, this paper introduces three significant contributions that stand apart from previous research:

1) It is widely recognized that obtaining accurate performance predictions through analytical models poses greater challenges for open-slot PMSMs, mainly due to significant leakage effects resulting from wide slot openings. Nevertheless, the coenergy-based analytical method proposed in this paper demonstrates remarkable accuracy, comparable to FEA, thereby highlighting its substantial research contribution.

2) The systematic separation has been performed between the components relevant and irrelevant to the optimization process. As a result, the optimization can be carried out without the necessity to compute the back-EMF and inductance. This approach effectively mitigates the time-consuming aspect of the coenergy-based method, which represents a notable advantage of the proposed approach.

3) The determination of the slot opening to slot pitch ratio is of paramount importance in the design of open-slot PMSMs. From this perspective, the optimal trend of the slot opening to slot pitch ratio, as presented in Figs. 6 and 7, proves highly advantageous, especially for the early design process, as it provides valuable guidelines for selecting appropriate values of the slot opening to slot pitch ratio.

APPENDIX

To solve ten unknown coefficients shown in (4)-(6), the derivation techniques presented in [38] and [45] are combined and adapted to the open-slot configuration. The five particular solutions shown in (4)-(6) can be specified as

$$\beta_{PMc} = \frac{\mu_0 r}{n^2-1}\left(M_{\theta cn} - nM_{rsn}\right) \tag{A.1}$$

$$\beta_{PMs} = \frac{\mu_0 r}{n^2-1}\left(M_{\theta sn} + nM_{rcn}\right) \tag{A.2}$$

$$\beta_{cu1} = \frac{\mu_0 r^2}{\Lambda_m^2-4} J_{im} \tag{A.3}$$

$$\beta_{cu2} = \frac{\mu_0 R_{sb}^2 \ln r}{2} J_{i0} \tag{A.4}$$

$$\beta_{cu3} = -\frac{\mu_0 r^2}{4} J_{i0} \tag{A.5}$$

where $M_{\theta cn}$, M_{rsn}, $M_{\theta sn}$, and M_{rcn} are given in [37] and J_{i0} and J_{im} are given in [45].

Applying the boundary condition $H_{1\theta}|_{r=R_r} = 0$, the following equations can be obtained by

$$A_1\left(\frac{R_r}{R_m}\right)^n - B_1 = -\frac{\mu_0 R_r}{n^2-1}\left(nM_{\theta cn} - M_{rsn}\right) \tag{A.6}$$

$$C_1\left(\frac{R_r}{R_m}\right)^n - D_1 = -\frac{\mu_0 R_r}{n^2-1}\left(nM_{\theta sn} + M_{rcn}\right) \tag{A.7}$$

Applying the boundary condition $B_{1r}|_{r=R_m} = B_{2r}|_{r=R_m}$, the following equations can be expressed by

$$\begin{aligned} &A_1 + B_1\left(\frac{R_r}{R_m}\right)^n - A_2\left(\frac{R_m}{R_s}\right)^n - B_2 \\ &\quad = -\frac{\mu_0 R_m}{n^2-1}\left(M_{\theta cn} - nM_{rsn}\right) \end{aligned} \tag{A.8}$$

$$\begin{aligned} &C_1 + D_1\left(\frac{R_r}{R_m}\right)^n - C_2\left(\frac{R_m}{R_s}\right)^n - D_2 \\ &\quad = -\frac{\mu_0 R_m}{n^2-1}\left(M_{\theta sn} + nM_{rcn}\right) \end{aligned} \tag{A.9}$$

Applying the boundary condition $H_{1\theta}|_{r=R_m} = H_{2\theta}|_{r=R_m}$, the following equations can be obtained as

$$\begin{aligned} &A_1 - B_1\left(\frac{R_r}{R_m}\right)^n - \mu_r A_2\left(\frac{R_m}{R_s}\right)^n + \mu_r B_2 \\ &\quad = -\frac{\mu_0 R_m}{n^2-1}\left(nM_{\theta cn} - M_{rsn}\right) \end{aligned} \tag{A.10}$$

$$\begin{aligned} &C_1 - D_1\left(\frac{R_r}{R_m}\right)^n - \mu_r C_2\left(\frac{R_m}{R_s}\right)^n + \mu_r D_2 \\ &\quad = -\frac{\mu_0 R_m}{n^2-1}\left(nM_{\theta sn} + M_{rcn}\right) \end{aligned} \tag{A.11}$$

Applying the boundary condition $H_{3\theta}|_{r=R_{sb}} = 0$, the following equations can be expressed as

$$A_{3i} - B_{3i}\left(\frac{R_s}{R_{sb}}\right)^{\Lambda_m} = -\frac{2\mu_0 R_{sb}^2 J_{ik}}{\Lambda_m\left(\Lambda_m^2-4\right)} \tag{A.12}$$

Applying the boundary condition $H_{2\theta}|_{r=R_s} = H_{3\theta}|_{r=R_s}$, the following equations can be obtained by

$$\begin{aligned} &nA_2 - nB_2\left(\frac{R_m}{R_s}\right)^n \\ &= -R_s\mu_0\left[\sum_i -\frac{J_{i0}}{2R_s}\left(R_{sb}^2 - R_s^2\right)\zeta_{i0}\right. \\ &\quad \left.+\sum_i\sum_m\left(-\frac{\Lambda_m}{R_s\mu_0}\left(A_{3i}\left(\frac{R_s}{R_{sb}}\right)^{\Lambda_m} - B_{3i}\right) - \frac{2R_s J_{im}}{\Lambda_m^2-4}\right)\zeta_i\right] \end{aligned} \tag{A.13}$$

$$\begin{aligned} &nC_2 - nD_2\left(\frac{R_m}{R_s}\right)^n \\ &= -R_s\mu_0\left[\sum_i -\frac{J_{i0}}{2R_s}\left(R_{sb}^2 - R_s^2\right)\xi_{i0}\right. \\ &\quad \left.+\sum_i\sum_m\left(-\frac{\Lambda_m}{R_s\mu_0}\left(A_{3i}\left(\frac{R_s}{R_{sb}}\right)^{\Lambda_m} - B_{3i}\right) - \frac{2R_s J_{im}}{\Lambda_m^2-4}\right)\xi_i\right] \end{aligned} \tag{A.14}$$

where ζ_{i0}, ζ_i, ξ_{i0}, and ξ_i are given by

$$\zeta_{i0} = \frac{2}{n\pi}\cos(n\theta_i)\sin\left(\frac{nb_{sa}}{2}\right) \tag{A.15}$$

$$\zeta_i = \frac{1}{\pi}\frac{n}{\Lambda_m^2 - n^2}\left[\sin\left(n\theta_i - \frac{nb_{sa}}{2}\right) - \cos(m\pi)\sin\left(n\theta_i + \frac{nb_{sa}}{2}\right)\right] \tag{A.16}$$

$$\xi_{i0} = \frac{2}{n\pi}\sin(n\theta_i)\sin\left(\frac{nb_{sa}}{2}\right) \tag{A.17}$$

$$\xi_i = \frac{1}{\pi}\frac{n}{\Lambda_m^2 - n^2}\left[\cos(m\pi)\cos\left(n\theta_i + \frac{nb_{sa}}{2}\right) - \cos\left(n\theta_i - \frac{nb_{sa}}{2}\right)\right] \tag{A.18}$$

Applying the boundary condition $B_{2r}|_{r=R_s} = B_{3r}|_{r=R_s}$, the following equations can be obtained by

$$A_{3i}\left(\frac{R_s}{R_{sb}}\right)^{\Lambda_m} - A_2\zeta_i\left(\frac{2\pi}{b_{sa}}\right) - B_2\left(\frac{R_m}{R_s}\right)^n\zeta_i\left(\frac{2\pi}{b_{sa}}\right) + B_{3i} - C_2\xi_i\left(\frac{2\pi}{b_{sa}}\right) - D_2\left(\frac{R_m}{R_s}\right)^n\xi_i\left(\frac{2\pi}{b_{sa}}\right) = -\frac{\mu_0 R_s}{\Lambda_m^2 - 4}J_{im} \tag{A.19}$$

Finally, the ten unknown coefficients (i.e., A_1, B_1, C_1, D_1, A_2, B_2, C_2, D_2, A_{3i}, and B_{3i}) can be determined by solving the multivariable equation set shown in (A.6), (A.7), (A.8), (A.9), (A.10), (A.11), (A.12), (A.13), (A.14), and (A.19).

REFERENCES

[1] L. Geng, F. Chai, and Y. Pei, "Mitigation of interturn short circuit fault based on axial split phase permanent magnet synchronous machine," *IEEE Trans. Energy Convers.*, vol. 37, no. 4, pp. 2578–2587, Dec. 2022.
[2] J. Ji, Y. Yang, Z. Ling, and W. Zhao, "Multi-objective optimization of interior permanent magnet machine for heavy-duty vehicle direct-drive applications," *IEEE Trans. Energy Convers.*, vol. 37, no. 3, pp. 1946–1954, Sep. 2022.
[3] G. Kucukyildiz, E. Yolacan, H. Ocak, and M. Aydin, "Detection of structural magnet defects for permanent magnet synchronous motors," *IEEE Trans. Energy Convers.*, vol. 37, no. 1, pp. 665–674, Mar. 2022.
[4] W. Tong, S. Li, X. Pan, S. Wu, and R. Tang, "Analytical model for cogging torque calculation in surface-mounted permanent magnet motors with rotor eccentricity and magnet defects," *IEEE Trans. Energy Convers.*, vol. 35, no. 4, pp. 2191–2200, Dec. 2020.
[5] S. G. Min, G. Bramerdorfer, and B. Sarlioglu, "Analytical modeling and optimization for electromagnetic performances of fractional-slot PM brushless machines," *IEEE Trans. Ind. Electron.*, vol. 65, no. 5, pp. 4017–4027, May 2018.
[6] A. M. El-Refaie, "Fractional-slot concentrated-windings synchronous permanent magnet machines: Opportunities and challenges," *IEEE Trans. Ind. Electron.*, vol. 57, no. 1, pp. 107–121, Jan. 2010.
[7] A. M. El-Refaie and T. M. Jahns, "Optimal flux weakening in surface PM machines using fractional-slot concentrated windings," *IEEE Trans. Ind. Appl.*, vol. 41, no. 3, pp. 790–800, May/Jun. 2005.
[8] S. G. Min and B. Sarlioglu, "Analysis and comparative study of flux weakening capability in fractional-slot concentrated windings," *IEEE Trans. Energy Convers.*, vol. 33, no. 3, pp. 1025–1035, Sep. 2018.
[9] D. Wu and Z. Q. Zhu, "Design tradeoff between cogging torque and torque ripple in fractional slot surface-mounted permanent magnet machines," *IEEE Trans. Magn.*, vol. 51, no. 11, pp. 1–4, Nov. 2015.
[10] T. Liu, S. Huang, J. Gao, and K. Lu, "Cogging torque reduction by slot-opening shift for permanent magnet machines," *IEEE Trans. Magn.*, vol. 49, no. 7, pp. 4028–4031, Jul. 2013.
[11] X. Ge, Z. Q. Zhu, G. Kemp, D. Moule, and C. Williams, "Optimal step-skew methods for cogging torque reduction accounting for three-dimensional effect of interior permanent magnet machines," *IEEE Trans. Energy Convers.*, vol. 32, no. 1, pp. 222–232, Mar. 2017.
[12] S. G. Min, "Investigation of key parameters on cogging torque in permanent magnet machines based on dominant harmonic contents," *IEEE Trans. Transport. Electrific.*, vol. 10, no. 1, pp. 174–186, Mar. 2024, doi: 10.1109/TTE.2023.3257842.
[13] A. J. P. Ortega and L. Xu, "Analytical prediction of torque ripple in surface-mounted permanent magnet motors due to manufacturing variations," *IEEE Trans. Energy Convers.*, vol. 31, no. 4, pp. 1634–1644, Dec. 2016.
[14] J. Zhou, M. Cheng, H. Wen, X. Yan, M. Tong, and W. Wang, "Modeling and suppression of torque ripple in PMSM based on the general airgap field modulation theory," *IEEE Trans. Power Electron.*, vol. 37, no. 10, pp. 12502–12512, Oct. 2022.
[15] J. M. Park, S. I. Kim, J. P. Hong, and J. H. Lee, "Rotor design on torque ripple reduction for a synchronous reluctance motor with concentrated winding using response surface methodology," *IEEE Trans. Magn.*, vol. 42, no. 10, pp. 3479–3481, Oct. 2006.
[16] W. Zhao, Z. Yang, Y. Liu, and X. Wang, "Analysis of a novel surface-mounted permanent magnet motor with hybrid magnets for low cost and low torque pulsation," *IEEE Trans. Magn.*, vol. 57, no. 6, pp. 1–4, Jun. 2021.
[17] J. Li, K. Wang, and C. Liu, "Torque improvement and cost reduction of permanent magnet machines with a dovetailed consequent-pole rotor," *IEEE Trans. Energy Convers.*, vol. 33, no. 4, pp. 1628–1640, Dec. 2018.
[18] R. Islam and I. Husain, "Analytical model for predicting noise and vibration in permanent-magnet synchronous motors," *IEEE Trans. Ind. Appl.*, vol. 46, no. 6, pp. 2346–2354, Nov/Dec. 2010.
[19] H. Yang and Y. Chen, "Influence of radial force harmonics with low mode number on electromagnetic vibration of PMSM," *IEEE Trans. Energy Convers.*, vol. 29, no. 1, pp. 38–45, Mar. 2014.
[20] W. Deng and S. Zuo, "Electromagnetic vibration and noise of the permanent-magnet synchronous motors for electric vehicles: An overview," *IEEE Trans. Transport. Electrific.*, vol. 5, no. 1, pp. 59–70, Mar. 2019.
[21] A. M. El-Refaie, T. M. Jahns, and D. W. Novotny, "Analysis of surface permanent magnet machines with fractional-slot concentrated windings," *IEEE Trans. Energy Convers.*, vol. 21, no. 1, pp. 34–43, Mar. 2006.
[22] M. Aydin, S. Huang, and T. A. Lipo, "Design, analysis, and control of a hybrid field-controlled axial-flux permanent-magnet motor," *IEEE Trans. Ind. Electron.*, vol. 57, no. 1, pp. 78–87, Jan. 2010.
[23] M.-F. Hsieh and Y.-C. Hsu, "A generalized magnetic circuit modeling approach for design of surface permanent-magnet machines," *IEEE Trans. Ind. Electron.*, vol. 59, no. 2, pp. 779–792, Feb. 2012.
[24] D.-K. Hong, W. Hwang, J.-Y. Lee, and B.-C. Woo, "Design, analysis, and experimental validation of a permanent magnet synchronous motor for articulated robot applications," *IEEE Trans. Magn.*, vol. 54, no. 3, pp. 1–4, Mar. 2018.
[25] S. G. Min and B. Sarlioglu, "Fast and systematic design optimization of surface-mounted PM machines using advanced analytical models and subharmonic elimination methods," *IEEE Trans. Magn.*, vol. 55, no. 1, pp. 1–16, Jan. 2019.
[26] J. Wang, X. Yuan, and K. Atallah, "Design optimization of a surface-mounted permanent-magnet motor with concentrated windings for electric vehicle applications," *IEEE Trans. Veh. Technol.*, vol. 62, no. 3, pp. 1053–1064, Mar. 2013.
[27] P. Asef, R. B. Perpiña, M. R. Barzegaran, A. Lapthorn, and D. Mewes, "Multiobjective design optimization using dual-level response surface methodology and Booth's algorithm for permanent magnet synchronous generators," *IEEE Trans. Energy Convers.*, vol. 33, no. 2, pp. 652–659, Jun. 2018.
[28] H. Guo, Z. Wu, H. Qian, and Z. Sun, "Robust design for the 9-slot 8-pole surface-mounted permanent magnet synchronous motor by analytical method-based multi-objectives particle swarm optimisation," *IET Electric Power Appl.*, vol. 10, no. 2, pp. 117–124, Feb. 2016.
[29] Z. Xue, H. Li, Y. Zhou, N. Ren, and W. Wen, "Analytical prediction and optimization of cogging torque in surface-mounted permanent magnet machines with modified particle swarm optimization," *IEEE Trans. Ind. Electron.*, vol. 64, no. 12, pp. 9795–9805, Dec. 2017.
[30] N. Bianchi, S. Bolognani, and E. Fomasiero, "A general approach to determine the rotor losses in three-phase fractional-slot PM machines," in *Proc. IEEE Int. Electric Mach. Drives Conf.*, May 2007, pp. 634–641.

[31] X. Fan, B. Zhang, R. Qu, D. Li, J. Li, and Y. Huo, "Comparative thermal analysis of IPMSMs with integral-slot distributed-winding (ISDW) and fractional-slot concentrated-winding (FSCW) for electric vehicle application," *IEEE Trans. Ind. Appl.*, vol. 55, no. 4, pp. 3577–3588, Jul. 2019.
[32] P. M. Lindh, H. K. Jussila, M. Niemela, A. Parviainen, and J. Pyrhonen, "Comparison of concentrated winding permanent magnet motors with embedded and surface-mounted rotor magnets," *IEEE Trans. Magn.*, vol. 45, no. 5, pp. 2085–2089, May 2009.
[33] R. Wrobel, P. H. Mellor, N. McNeill, and D. A. Staton, "Thermal performance of an open-slot modular-wound machine with external rotor," *IEEE Trans. Energy Convers.*, vol. 25, no. 2, pp. 403–411, Jun. 2010.
[34] R. Wrobel and P. H. Mellor, "Design considerations of a direct drive brushless machine with concentrated windings," *IEEE Trans. Energy Convers.*, vol. 23, no. 1, pp. 1–8, Mar. 2008.
[35] R. Wrobel, J. Goss, A. Mlot, and P. H. Mellor, "Design considerations of a brushless open-slot radial-flux PM hub motor," *IEEE Trans. Ind. Appl.*, vol. 50, no. 3, pp. 1757–1767, May/Jun. 2014.
[36] F. Dubas and C. Espanet, "Analytical solution of the magnetic field in permanent-magnet motors taking into account slotting effect: No-load vector potential and flux density calculation," *IEEE Trans. Magn.*, vol. 45, no. 5, pp. 2097–2109, May 2009.
[37] Z. Q. Zhu, L. J. Wu, and Z. P. Xia, "An accurate subdomain model for magnetic field computation in slotted surface-mounted permanent-magnet machines," *IEEE Trans. Magn.*, vol. 46, no. 4, pp. 1100–1115, Apr. 2010.
[38] L. J. Wu, Z. Q. Zhu, D. Staton, M. Popescu, and D. Hawkins, "An improved subdomain model for predicting magnetic field of surface-mounted permanent magnet machines accounting for tooth-tips," *IEEE Trans. Magn.*, vol. 47, no. 6, pp. 1693–1704, Jun. 2011.
[39] D. Zarko, D. Ban, and T. A. Lipo, "Analytical calculation of magnetic field distribution in the slotted air gap of a surface permanent-magnet motor using complex relative air-gap permeance," *IEEE Trans. Magn.*, vol. 42, no. 7, pp. 1828–1837, Jul. 2006.
[40] D. Zarko, D. Ban, and T. A. Lipo, "Analytical solution for cogging torque in surface permanent-magnet motors using conformal mapping," *IEEE Trans. Magn.*, vol. 44, no. 1, pp. 52–65, Jan. 2008.
[41] S. G. Min and B. Sarlioglu, "Analytical calculation of back EMF waveform for linear PM motors in slotted and slotless structures," *IEEE Trans. Magn.*, vol. 53, no. 12, pp. 1–10, Dec. 2017.
[42] R. V. Rao, V. J. Savsani, and D. P. Vakharia, "Teaching–learning-based optimization: A novel method for constrained mechanical design optimization problems," *Comput.-Aided Des.*, vol. 43, no. 3, pp. 303–315, Mar. 2011.
[43] Z. Q. Zhu, D. Howe, and C. C. Chan, "Improved analytical model for predicting the magnetic field distribution in brushless permanent-magnet machines," *IEEE Trans. Magn.*, vol. 38, no. 1, pp. 229–238, Jan. 2002.
[44] D. C. Hanselman, *Brushless Permanent Magnet Motor Design*. New York, NY, USA: McGraw-Hill, 2003.
[45] L. J. Wu, Z. Q. Zhu, D. Staton, M. Popescu, and D. Hawkins, "Subdomain model for predicting armature reaction field of surface-mounted permanent-magnet machines accounting for tooth-tips," *IEEE Trans. Magn.*, vol. 47, no. 4, pp. 812–822, Apr. 2011.

DO HYEON LEE (Student Member, IEEE) received the B.S. degree in electrical engineering from the Electrical Machines and Optimization Data Analysis Laboratory (EMODAL), Soongsil University, Seoul, South Korea, in 2024.

His research interests include design, analysis, and optimization of electric machine based on meta-heuristic algorithms.

SEUN GUY MIN (Member, IEEE) received the B.S. degree in electrical engineering from Iowa State University, Ames, IA, USA, in 2010, and the M.S. and Ph.D. degrees in electrical engineering from Wisconsin Electric Machines and Power Electronics Consortium (WEMPEC), University of Wisconsin, Madison, WI, USA, in 2013 and 2019, respectively.

From 2013 to 2016, he worked in the industry as the General Manager of the Electrical Machine Division of Research and Development, JUSTEK, Gyeonggi-do, South Korea. Since 2019, he has been an Assistant Professor with Soongsil University, Seoul, South Korea. During the Ph.D. degree, he has authored ten IEEE journal articles as the primary contributor, marking the highest number of first-author IEEE TRANSACTIONS articles published by any individual affiliated with WEMPEC since its inception, in 1981, with over 700 graduate students. His research interests include analysis, design, modeling, optimization of electric machines, integrated electro-mechanical solutions for linear motion devices, predictive analytics and forecasting using machine/deep learning, and optimization data analysis based on robust evolutionary algorithms.